Strain-engineered magnon states in two-dimensional ferromagnetic monolayers

Bin Wei [1], Jia-Ji Zhu [2,3,*], Yun Song [4,†] and Kai Chang [1,5,‡]

[1] *SKLSM, Institute of Semiconductors,Chinese Academy of Sciences, Beijing 100083, China*

[2] *School of Science and Institute for Advanced Sciences, Chongqing University of Posts and Telecommunications, Chongqing 400061, China*

[3] *Southwest Center for Theoretical Physics, Chongqing University, Chongqing 401331, China*

[4] *Department of Physics, Beijing Normal University, Beijing 100875, China*

[5] *School of Physics, Zhejiang University, Hangzhou 310027, China*

(Received 22 September 2023; accepted 25 January 2024; published 27 February 2024)

We systematically investigate the strain-engineered magnon states in two-dimensional (2D) ferromagnetic monolayers. By suitable engineering of an inhomogeneous strain, we demonstrate the emergence of magnon Landau levels and magnon snake states in 2D ferromagnetic monolayers. We show a magnon valley Hall effect and valley filter without relying on any external fields. Our proposal offers us another way to manipulate magnon valley transport and construct different types of flexible spintronic devices, and is experimentally feasible for 2D ferromagnetic materials by using state-of-art techniques.

DOI: 10.1103/PhysRevResearch.6.013210

I. INTRODUCTION

Strain engineering is an efficient strategy for tuning the properties of materials and exploring new quantum states in condensed matter physics [1]. In the case of an electronic system, strain has been tailored to tune the electronic structure [2–4], alter the topology [5–10], generate valley-polarized currents [11–14], and develop next-generation devices for information [15,16].

Magnons, which are ideal information carriers that can carry and process information over several millimeters without Joule heat, are currently regaining attention due to the experimental fabrication of various atomically thin magnetic crystals [17–20]. Research on magnons has inspired a plethora of interesting results, such as topological magnons [21–24], magnon Bose-Einstein condensates [25], the magnon Hall effect [26,27], and Dirac magnons [28,29].

Magnons in two-dimensional (2D) magnetic materials display unique characteristics, such as lower-energy dissipation, terahertz frequencies, and strong anisotropy, making them ideal candidates for flexible and high-frequency devices [30]. However, conventional periodic modulations, for example, patterning, and thickness modification, are no longer applicable for controlling the dynamic behavior of magnons in 2D systems. Therefore, strain becomes the primary approach to engineer magnon states, which attracts increasing interest in magnon straintronics in 2D van der Waals magnetic materials [31,32].

In this paper, we systematically study the strain-engineered magnon states for symmetric and antisymmetric strain in an armchair or zigzag ribbon, as shown in Fig. 1. The strain generates a pseudomagnetic field (PMF) and induces magnon Landau levels (LLs). Magnon snake states can be realized locally in the middle of a ferromagnetic ribbon by engineering an inhomogeneous strain. In a zigzag ribbon, we demonstrate a magnon valley Hall effect (VHE) under experimentally available strain profiles. Inhomogeneous strain generates a valley-dependent PMF at the K valleys, whose orientation is opposite to the PMF at the K' valleys, resulting in valley-dependent edge states. As such, strain can be employed as a straightforward and efficient method for fabricating magnon valley filters.

II. SPIN-WAVE THEORY

The Hamiltonian considered in this paper is based on the magnetic description of a spin-3/2 ferromagnetic CrI_3 monolayer, where the magnetic ions Cr^{3+} form a honeycomb lattice and exhibit ferromagnetic long-range order with an out-of-plane easy axis [33–35]. We consider the anisotropic Heisenberg Hamiltonian

$$H = -\frac{1}{2}\sum_{\langle i,j\rangle}(J\mathbf{S}_i\cdot\mathbf{S}_j + \lambda\mathbf{S}_i^z\mathbf{S}_j^z), \tag{1}$$

where $\langle i, j\rangle$ denotes a summation over the nearest-neighbor sites. The first and second terms represent the isotropic and anisotropic exchange interactions, respectively. We neglect the contribution of single-ion anisotropic interactions and

*zhujj@cqupt.edu.cn
†yunsong@bnu.edu.cn
‡kchang@semi.ac.cn

dipole-dipole interactions because they are small and only slightly shift the magnon spectrum.

By applying the Dyson-Maleev transformation [36–38] $S_i^+ = \sqrt{2S}(1 - a_i^\dagger a_i/2S)a_i$, $S_i^- = \sqrt{2S}a_i^\dagger$, $S_i^z = S - a_i^\dagger a_i$, the spatial-Fourier transformation, and canonical transformation, the Hamiltonian can be expressed as

$$H = \frac{(J+\lambda)}{2}NZS^2 + \sum_k (E_k^+ \alpha_k^\dagger \alpha_k + E_k^- \beta_k^\dagger \beta_k), \quad (2)$$

with

$$E_k^\pm = \frac{(J+\lambda)}{2}SZ \pm \frac{JSZ}{4}\sqrt{3+f(k)}, \quad (3)$$

$$f(k) = 2\cos(\sqrt{3}a_0 k_y) + 4\cos\left(\frac{\sqrt{3}}{2}a_0 k_y\right)\cos\left(\frac{\sqrt{3}}{2}a_0 k_x\right), \quad (4)$$

where a_0 is the magnetic lattice constant, and $Z = 3$ is the coordination number. The exchange interaction parameters, $J = 2.7$ meV and $\lambda = 0.11$ meV, are from experiments [39]. (The spectrum is available in the Supplemental Material [40].) The Hamiltonian is approximated to second order in the magnon operators. Although the higher-order terms lead to softening effects, they preserve the relevant symmetries and therefore do not destroy the Dirac magnon properties [29,41,42]. We map the magnonic system onto an effective Hamiltonian as

$$H = \sum_{\langle i \rangle} t_0 (a_i^\dagger a_i + b_i^\dagger b_i) + \sum_{\langle i,j \rangle} (t_{ij} a_i b_j^\dagger + \text{H.c.}), \quad (5)$$

where t_0 (t_{ij}) represents the on-site energy (hopping integral). An external mechanical strain that varies smoothly on the scale of interatomic distances modifies the hopping integral between different sites. This does not break the sublattice symmetry but instead shifts the Dirac cones at points K and K' in opposite directions. An inhomogeneous strain can produce a nonvanishing PMF, whereas a homogenous strain will not. A 2D inhomogeneous strain leads to the gauge field [43]

$$A = \frac{\tau_z \beta}{2a_0}\begin{pmatrix} u_{xx} - u_{yy} \\ -2u_{xy} \end{pmatrix}, \quad (6)$$

where $\beta \approx 2$ is a dimensionless constant for CrI_3. $\tau_z = \pm$ denote two inequivalent valleys in the Brillouin zone. The strain tensor components are given by

$$u_{xx} = \frac{\partial u_x}{\partial x} + \frac{1}{2}\left(\frac{\partial h}{\partial x}\right)^2,$$
$$u_{xy} = \frac{1}{2}\left(\frac{\partial u_x}{\partial y} + \frac{\partial u_y}{\partial x}\right) + \frac{1}{2}\left(\frac{\partial h}{\partial x} + \frac{\partial h}{\partial y}\right),$$
$$u_{yy} = \frac{\partial u_y}{\partial y} + \frac{1}{2}\left(\frac{\partial h}{\partial y}\right)^2. \quad (7)$$

The coordinate system is defined as the x axis along the zigzag direction. We propose several strain forms, which can produce a strictly uniform PMF in the armchair or zigzag edges. Here, we choose the strain forms $u_y = C_s x^2$ for the armchair ribbon and $u_y = C_s y^2$ for the zigzag ribbon, respectively. C_s is the strength of the strain. By translating to a PMF, we get

$$\mathbf{B}_{\text{eff}} = -\tau_z \beta C_s \mathbf{e}_z / a_0. \quad (8)$$

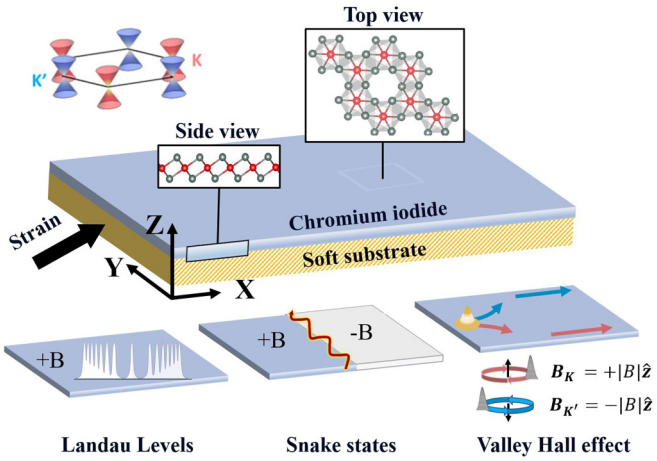

FIG. 1. Schematic diagram of strain-engineered magnon states. The 2D magnetic monolayer, e.g., CrI_3, is placed on a soft substrate. By employing symmetric and antisymmetric strain, magnon Landau levels and snake states arise in the armchair and zigzag ribbons. The strain-induced pseudomagnetic fields point in the $\pm z$ direction for different valleys in the zigzag ribbon. The magnon valley Hall effect emerges, denoted by the blue and red arrows indicating the drift of magnon wave packets to the upper and lower edges of the system, respectively.

Note that the PMF has opposite sign at different valleys. Magnon LLs are given by

$$E_n = \frac{SZ(J+\lambda)}{2} + \text{sgn}(n)\omega\sqrt{|n|}, \quad (9)$$

where n is the LL index, $\omega = 3t_{ij}\sqrt{2\beta C_s a_0}/2$. Both in magnon systems and strained graphene, the PMF causes Landau-level quantization. However, the real magnetic field behaves differently in these two systems. In magnonic systems, the real magnetic field shifts the magnon spectrum through the Zeeman interaction, whereas in strained graphene it also produces Landau levels.

III. MAGNON LLs AND VHE

We investigate valley-polarized magnons in an 800-nm-wide zigzag ribbon of monolayer CrI_3. Under a strain-free condition shown in Fig. 2(a), the magnon spectrum exhibits two Dirac cones connected by the flat edge states. Figure 2(b) shows the magnon LLs generated by the PMF when the inhomogeneous strain is imposed on the ribbon. The magnons at the K and K' valleys are pushed to different edges, forming the valley magnon edge states. The upper branches are propelled towards the Dirac frequency, and the corresponding wave function [see the inset of Fig. 2(b)] indeed localizes at the edge of the ribbon. The flat band corresponds to trivial edge states associated with the zigzag edge, connecting the K and K' valleys. The $n = 0$ magnon Landau level is degenerate with trivial edge states on both zigzag edges. The zigzag edge states remain unaltered by the implementation of inhomogeneous strain. Away from the K and K' points, the $n = 0$ magnon Landau level evolves into two split bands. Higher-order ($|n| > 0$) magnon LLs with a linear dispersion near the Dirac frequency are also shown in Fig. 2(c). The blue circles represent the

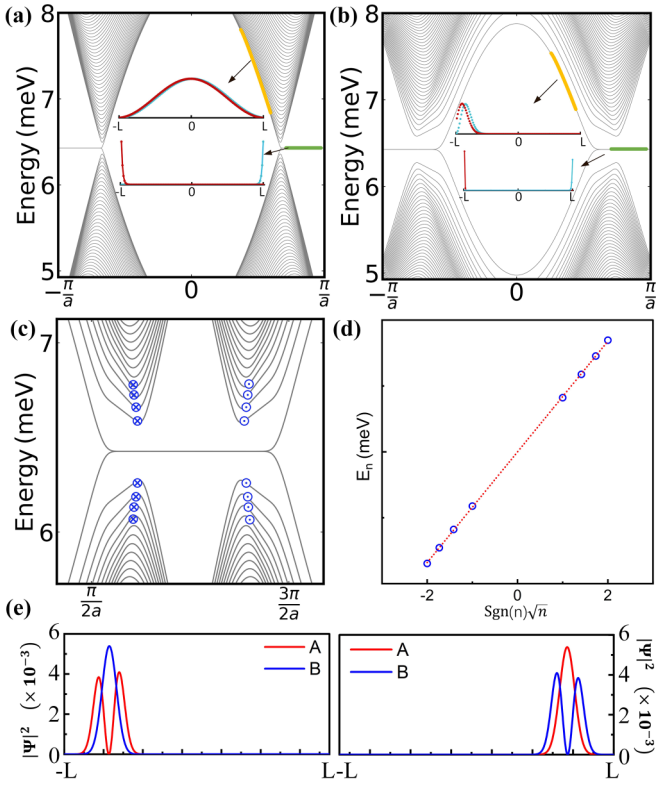

FIG. 2. The magnon spectrum of the zigzag ribbon with different strain strengths (a) $C_s = 0$ and (b) $C_s = 0.2 \times 10^{-3}/a_0$. Gray lines depict numerical results for all the magnon bands, and the thick yellow (green) line segments depict the representative bulk (edge) state. The insets show the wave-function spatial distributions for corresponding states. The blue and red lines represent the A sublattice and B sublattice, respectively. (c) The magnon spectrum near the Dirac frequency, where the magnon LLs emerge. The blue circles indicate the magnon LLs $n = \pm1, \pm2, \pm3$, and ±4. The symbols $\otimes$ and $\odot$ denote the signs of the PMFs. (d) The energies of magnon LLs depend on the index (n) of the LLs. The blue circles correspond to the blue circles in (c), and the red dotted line is the theoretical fitting by Eq. (9). (e) The wave-function spatial distributions for K and K' valleys of the first magnon LLs.

first few magnon LLs defined by Eq. (9). Note that there is a tilt arising from the deformation potential. The tilt has the opposite sign for the magnon LLs splitting off the upper and lower branches. In addition, for the same branches with the same magnon LL index n, magnon LLs at opposite valleys are tilted in image orientations. We can see from Fig. 2(d) that our results agree well with the square-root n relation, which is the verification of the well-defined Landau quantization.

In addition to Landau quantization, a strong PMF also leads to magnon VHE, which originates from extra valley edge states. Figure 2(e) displays the spatial distribution of wave functions of magnon valley edge states along the ribbon. Indeed, these valley-dependent edge states are confined within a narrow area at different sides. The generated edge states circulate in opposite directions, since PMF has opposite signs in valleys K and K'. Compared to the edge states from zigzag edges, the pure valley edge currents are robust to disorders such as defects and reconstructions.

In contrast to the zigzag ribbon, the armchair ribbon has no edge state. Our calculation indicates that there would not be any Landau quantization and edge states without strain. Figure 3(a) shows the magnon spectra of the armchair ribbon for two different widths in the region $|k| \leqslant \pi/2a$. The top of the lower branches and the bottom of the upper branches are located at $k = 0$. The ribbon width determines whether the system is gapless, which is also a well-known phenomenon in graphene. As shown in the right panel, the system is gapless on $N = 3M - 1$, where M is an integer.

The strain drives the magnon states to the Landau quantization. Figure 3(b) shows the magnon spectra of the strained 822-nm-wide armchair ribbon. Well-resolved magnon LLs can be found when the magnetic length $l_B = 1/\sqrt{B_{\text{eff}}}$ is smaller than the width of the ribbon. The red dots represent the magnon LLs with $n = 0$, ±1, ±2, ±3, and ±4. The magnon LL energy increases with increasing Landau-level index and possesses a square-root relation with a Landau-level index n. (For more details, see Supplemental Material [40].) Unlike the zigzag ribbon, there is no linear tilt in the magnon LLs. The right panel depicts the magnon density of states, where the peaks correspond to the first few magnon LLs.

An armchair ribbon does not exhibit magnon VHE and valley-polarized edge states because the K' valley is degenerate with the K valley. However, the presence of PMF still results in edge states. As clearly shown in Fig. 3(c), the wave functions are propelled toward the edges as k increases. This is because the magnon energy increases due to the potential barrier imposed by the edges, once the magnon states meet the edges.

IV. MAGNON SNAKE STATES

In the case of magnon LLs and VHE, the PMF conserves cylindrical symmetry around the line along the y axis. However, we can construct antisymmetric strain with the distortion vector given by

$$\text{armchair ribbon}: \quad u_y = \begin{cases} C_s x^2, & x \geqslant 0, \\ -C_s x^2, & x < 0, \end{cases} \tag{10}$$

$$\text{zigzag ribbon}: \quad u_y = \begin{cases} C_s y^2, & y \geqslant 0, \\ -C_s y^2, & y < 0. \end{cases} \tag{11}$$

In this case, the orientation of the PMF on the two sides of the ribbon is opposite, which produces a PMF interface at the middle of the ribbon. The magnon spectrum corresponding to the antisymmetric strain is shown in Figs. 4(a) and 4(b) for the armchair ribbon (zigzag ribbon). We find new magnon states which have snake orbits arising from the PMF configuration. The magnon wave packets near the interface of the PMF do not evolve into closed trajectories, but into snake-like orbits. Furthermore, within the zigzag ribbon, magnons originating from distinct valleys exhibit opposing snake-state propagation directions at the interface. The snake states were also found in an electronic system [13]. The features of the snake states can be identified in the sublattice wave-function distributions, illustrated by dots marked with S in the insets of Figs. 4(a) and 4(b). The wave functions of snake states exhibit a symmetric distribution with respect to the interface

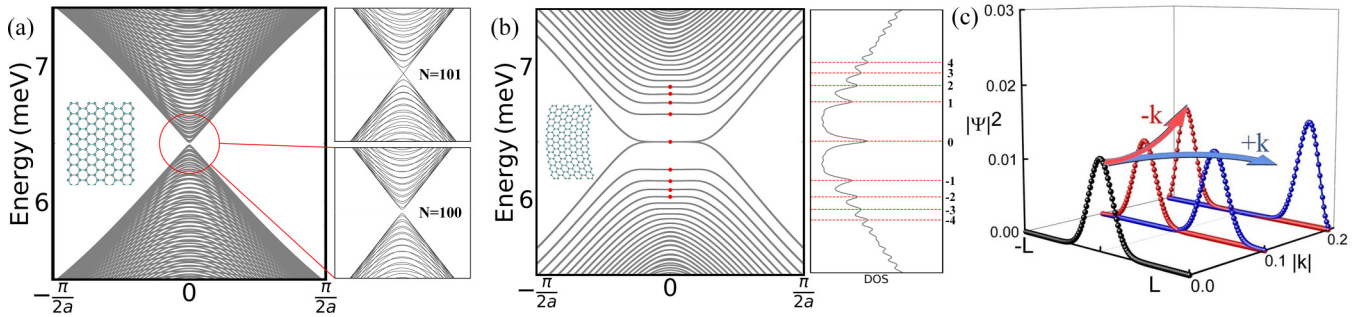

FIG. 3. (a) The magnon spectrum of the strain-free armchair ribbon with different widths $N = 100$ and 101. (b) The magnon spectrum and density of states of an 822-nm-wide armchair ribbon at strain strength $C_s = 0.3 \times 10^{-3}/a_0$, where $t_0 = 6.43$. The red dots and dashed lines in (b) indicate the magnon LLs $n = 0, \pm1, \pm2, \pm3, \pm4$ according to Eq. (9) with $B_{eff} = 2.53$ T. (c) Distribution of zeroth magnon LLs at $k = 0$, $|k| = 0.1\pi/a_0$, and $|k| = 0.2\pi/a_0$. At finite k, the magnons are pushed toward the edges due to the PMF induced by the inhomogeneous strain.

and are clearly spatially distinct from the edge states. In addition, the antisymmetric strain-induced PMF forces the guiding centers to opposite edges at the same crystal momentum k. These features can be identified in the spatial distribution of magnon edge states, as illustrated by dots marked with E in the insets. The dot marked with M is a quadruple-degenerate energy point, corresponding to mixed magnon states (the $n = 0$ magnon Landau level and edge states).

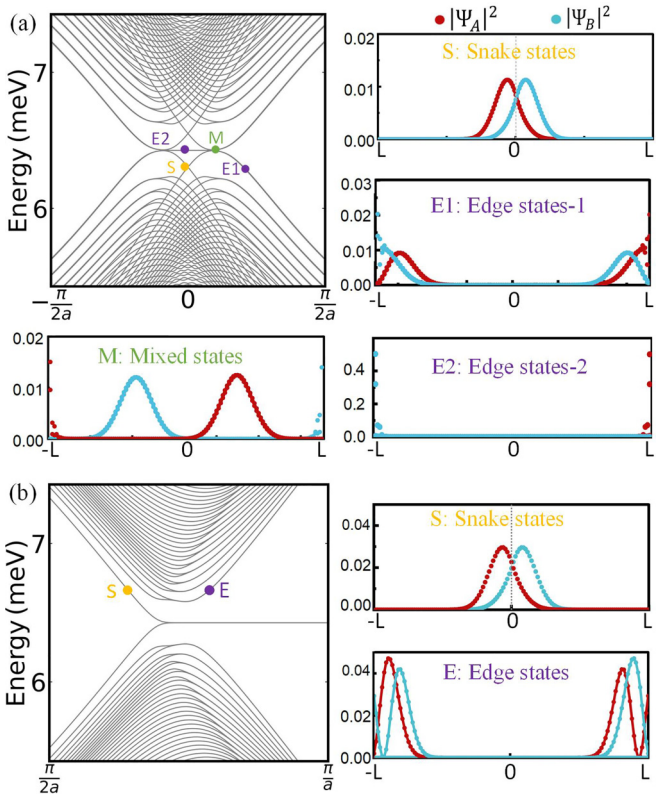

FIG. 4. The magnon spectrum of (a) the armchair ribbon and (b) the zigzag ribbon, with $C_s = 0.3 \times 10^{-3}/a_0$, respectively. The probability densities of the magnon states are illustrated in the insets, where the dots marked with S, $E1$, $E2$, and M correspond to magnon snake states, edge states, and mixed states. Ψ_A (red line) and Ψ_B (blue line) represent the two sublattices.

V. MAGNON VALLEY FILTER

We can realize valleytronic device applications by valley-polarized magnon current carrying a specific valley index, as illustrated in Fig. 5(a). In our proposal, magnons from different valleys feel the opposite PMF and propagate in opposite directions. We neglect the contribution of the Dzyaloshinskii-Moriya interaction in PMF. The Dzyaloshinskii-Moriya interaction in our system is significantly smaller than both the exchange interaction and the anisotropic exchange interaction, measuring two and one orders of magnitude smaller, respectively [44]. Only K-valley magnons can transmit through the bump, whereas the K'-valley magnons are immediately reflected. Therefore, a K-valley-polarized magnon current is generated at the opposite side of the bump. We can also generate a K'-valley-polarized magnon current by reversing the injection direction. Such a bump can be realized by magnetic materials over patterned holes on a SiO_2/Si substrate, where a uniform pressure difference can be produced under the magnetic materials and the bump bulges upwards in a controllable manner [45]. Figure 5(b) demonstrates the magnon valley filter with the PMF distribution for a Gaussian bump. We show

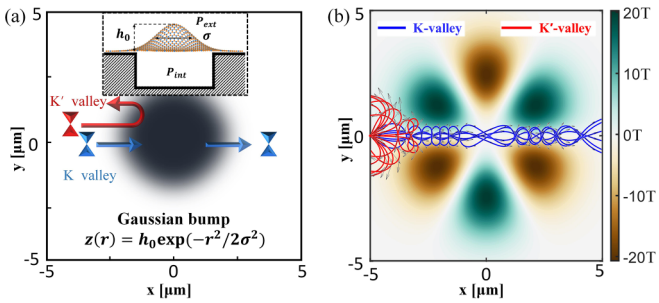

FIG. 5. (a) Schematic drawing of a magnon valley filter in the ferromagnetic monolayer with a Gaussian bump, where h_0 is the maximal deformation in the z direction and σ is the width of the Gaussian bump. The blue (red) arrows represent the K-valley (K'-valley) polarized magnons. The inset shows a CrI_3-sealed microcavity in the pressure chamber. (b) Profile of the pseudomagnetic field induced by a Gaussian bump in the K valley, where height $h_0 = 0.5$ μm, and width $\sigma = 3$ μm. Blue (red) lines are the K- (K'-) valley magnon trajectories incident from the left.

several typical magnon trajectories with different incidence angles, exhibiting a remarkable valley dependence. We can see that the K'-valley magnons are backscattered, whereas those from the K valley are transmitted.

VI. DISCUSSION AND CONCLUSION

Although challenging, we believe the proposed magnon LLs, snake states, and magnon VHE can be observed with present-day technology. Layered ferromagnetic monolayers, such as CrI_3, which have been prepared experimentally, can be placed on a soft substrate to apply the designed strain. The needed techniques have already been realized in graphene and other nonmagnetic 2D materials [14,46–49]. A magnetic field difference ΔB between the two sides of the system can provide effective chemical potentials for the magnons, which results in a magnon transport current. The magnon currents can be calculated from the Landauer-Büttiker theory [50] as

$$I_m = \int_{E-g\mu_B\Delta B/2}^{E+g\mu_B\Delta B/2} n_B(E)\Delta B dE = G_m \Delta B, \qquad (12)$$

where $n_B(E) = (e^{E/k_BT} - 1)^{-1}$ is the Bose-Einstein distribution, and $G_m = (g\mu_B)^2 n_B(E)/h$ is the magnon conductance. Because the magnon carries a spin degree of freedom, one may detect the magnon transport by measuring the spin conductance $G_s = \hbar G_m$ using Brillouin light scattering techniques. The magnon spectrum can be measured with inelastic neutron scattering.

In conclusion, we have systematically investigated the strain-engineered magnon states in 2D strained ferromagnetic ribbons, emphasizing the pivotal role of the type of strain and edge in shaping the magnon spectrum. We demonstrated that the magnon LLs and edge states emerge under symmetrical strain in the zigzag and armchair ribbon. We found unique magnon snake states by applying an antisymmetric strain configuration. A symmetrical strain can also induce VHE and valley-polarized edge states in a zigzag ribbon. However, the VHE and valley-polarized edge states are absent in the armchair ribbon due to the degeneracy of the K and K' valleys. We can implement valley-filtering and valley-splitting devices by utilizing the strain-engineered magnons. Our results enable a different scheme to control the magnon spectrum and transport properties, shedding light on the design of flexible magnonic devices.

ACKNOWLEDGMENTS

We thank D. Zhang for helpful discussions. This work is supported by the Strategic Priority Research Program of the Chinese Academy of Sciences (Grants No. XDB0460000 and No. XDB28000000), the National Natural Science Foundation of China (NSFC) (Grants No. 12247115, No. 12147382, No. 11974339, No. 92265203, and No. 11974340), the Ministry of Science and Technology of the People's Republic of China (Grant No. 2018YFA0306101), and the Research Foundation of Institute for Advanced Sciences of CQUPT (Grant No. E011A2022328).

[1] E. J. Johnson, Optical orientation in semiconductors, in *Theoretical Aspects and New Developments in Magneto-Optics*, edited by J. T. Devreese (Springer, Boston, MA, 1980), pp. 419–446.

[2] V. M. Pereira and A. H. C. Neto, Strain engineering of graphene's electronic structure, Phys. Rev. Lett. **103**, 046801 (2009).

[3] N. Levy, S. A. Burke, K. L. Meaker, M. Panlasigui, A. Zettl, F. Guinea, A. H. C. Neto, and M. F. Crommie, Strain-induced pseudo-magnetic fields greater than 300 tesla in graphene nanobubbles, Science **329**, 544 (2010).

[4] F. Guinea, M. I. Katsnelson, and A. K. Geim, Energy gaps and a zero-field quantum Hall effect in graphene by strain engineering, Nat. Phys. **6**, 30 (2010).

[5] M. S. Miao, Q. Yan, C. G. Van de Walle, W. K. Lou, L. L. Li, and K. Chang, Polarization-driven topological insulator transition in a GaN/InN/GaN quantum well, Phys. Rev. Lett. **109**, 186803 (2012).

[6] Z. Zhu, Y. Cheng, and U. Schwingenschlögl, Topological phase transition in layered GaS and GaSe, Phys. Rev. Lett. **108**, 266805 (2012).

[7] H. Yang, S. W. Kim, M. Chhowalla, and Y. H. Lee, Structural and quantum-state phase transitions in van der Waals layered materials, Nat. Phys. **13**, 931 (2017).

[8] F. Schindler, A. M. Cook, M. G. Vergniory, Z. Wang, S. S. P. Parkin, B. A. Bernevig, and T. Neupert, Higher-order topological insulators, Sci. Adv. **4**, eaat0346 (2018).

[9] J. Mutch, W.-C. Chen, P. Went, T. Qian, I. Z. Wilson, A. Andreev, C.-C. Chen, and J.-H. Chu, Evidence for a strain-tuned topological phase transition in $ZrTe_5$, Sci. Adv. **5**, eaav9771 (2019).

[10] P. D. C. King, Controlling topology with strain, Nat. Mater. **20**, 1046 (2021).

[11] O. Gunawan, Y. P. Shkolnikov, K. Vakili, T. Gokmen, E. P. De Poortere, and M. Shayegan, Valley susceptibility of an interacting two-dimensional electron system, Phys. Rev. Lett. **97**, 186404 (2006).

[12] Z. Wu, F. Zhai, F. M. Peeters, H. Q. Xu, and K. Chang, Valley-dependent Brewster angles and Goos-Hänchen effect in strained graphene, Phys. Rev. Lett. **106**, 176802 (2011).

[13] D.-B. Zhang, G. Seifert, and K. Chang, Strain-induced pseudomagnetic fields in twisted graphene nanoribbons, Phys. Rev. Lett. **112**, 096805 (2014).

[14] S.-Y. Li, Y. Su, Y.-N. Ren, and L. He, Valley polarization and inversion in strained graphene via pseudo-Landau levels, valley splitting of real Landau levels, and confined states, Phys. Rev. Lett. **124**, 106802 (2020).

[15] Y. Kato, R. C. Myers, A. C. Gossard, and D. D. Awschalom, Coherent spin manipulation without magnetic fields in strained semiconductors, Nature (London) **427**, 50 (2004).

[16] R. Roldán, A. Castellanos-Gomez, E. Cappelluti, and F. Guinea, Strain engineering in semiconducting two-dimensional crystals, J. Phys.: Condens. Matter **27**, 313201 (2015).

[17] C. Gong, L. Li, Z. Li, H. Ji, A. Stern, Y. Xia, T. Cao, W. Bao, C. Wang, Y. Wang, Z. Q. Qiu, R. J. Cava, S. G. Louie, J. Xia, and X. Zhang, Discovery of intrinsic ferromagnetism in two-dimensional van der Waals crystals, Nature (London) **546**, 265 (2017).

[18] B. Huang, G. Clark, E. Navarro-Moratalla, D. R. Klein, R. Cheng, K. L. Seyler, D. Zhong, E. Schmidgall, M. A. McGuire, D. H. Cobden, W. Yao, D. Xiao, P. Jarillo-Herrero, and X. Xu, Layer-dependent ferromagnetism in a van der Waals crystal down to the monolayer limit, Nature (London) **546**, 270 (2017).

[19] Z. Fei, B. Huang, P. Malinowski, W. Wang, T. Song, J. Sanchez, W. Yao, D. Xiao, X. Zhu, A. F. May, W. Wu, D. H. Cobden, J.-H. Chu, and X. Xu, Two-dimensional itinerant ferromagnetism in atomically thin Fe_3GeTe_2, Nat. Mater. **17**, 778 (2018).

[20] M. M. Otrokov, I. I. Klimovskikh, H. Bentmann, D. Estyunin, A. Zeugner, Z. S. Aliev, S. Gaß, A. U. B. Wolter, A. V. Koroleva, A. M. Shikin, M. Blanco-Rey, M. Hoffmann, I. P. Rusinov, A. Y. Vyazovskaya, S. V. Eremeev, Y. M. Koroteev, V. M. Kuznetsov, F. Freyse, J. Sánchez-Barriga, I. R. Amiraslanov *et al.*, Prediction and observation of an antiferromagnetic topological insulator, Nature (London) **576**, 416 (2019).

[21] R. Chisnell, J. S. Helton, D. E. Freedman, D. K. Singh, R. I. Bewley, D. G. Nocera, and Y. S. Lee, Topological magnon bands in a kagome lattice ferromagnet, Phys. Rev. Lett. **115**, 147201 (2015).

[22] S. A. Owerre, A first theoretical realization of honeycomb topological magnon insulator, J. Phys.: Condens. Matter **28**, 386001 (2016).

[23] Y.-M. Li, J. Xiao, and K. Chang, Topological magnon modes in patterned ferrimagnetic insulator thin films, Nano Lett. **18**, 3032 (2018).

[24] A. T. Costa, D. L. R. Santos, N. M. R. Peres, and J. Fernández-Rossier, Topological magnons in CrI_3 monolayers: An itinerant fermion description, 2D Mater. **7**, 045031 (2020).

[25] S. O. Demokritov, V. E. Demidov, O. Dzyapko, G. A. Melkov, A. A. Serga, B. Hillebrands, and A. N. Slavin, Bose–Einstein condensation of quasi-equilibrium magnons at room temperature under pumping, Nature (London) **443**, 430 (2006).

[26] Y. Onose, T. Ideue, H. Katsura, Y. Shiomi, N. Nagaosa, and Y. Tokura, Observation of the magnon Hall effect, Science **329**, 297 (2010).

[27] M. Mochizuki, X. Z. Yu, S. Seki, N. Kanazawa, W. Koshibae, J. Zang, M. Mostovoy, Y. Tokura, and N. Nagaosa, Thermally driven ratchet motion of a skyrmion microcrystal and topological magnon Hall effect, Nat. Mater. **13**, 241 (2014).

[28] J. Fransson, A. M. Black-Schaffer, and A. V. Balatsky, Magnon Dirac materials, Phys. Rev. B **94**, 075401 (2016).

[29] S. S. Pershoguba, S. Banerjee, J. C. Lashley, J. Park, H. Ågren, G. Aeppli, and A. V. Balatsky, Dirac magnons in honeycomb ferromagnets, Phys. Rev. X **8**, 011010 (2018).

[30] A. Barman, G. Gubbiotti, S. Ladak, A. O. Adeyeye, M. Krawczyk, J. Gräfe, C. Adelmann, S. Cotofana, A. Naeemi, V. I. Vasyuchka, B. Hillebrands, S. A. Nikitov, H. Yu, D. Grundler, A. V. Sadovnikov, A. A. Grachev, S. E. Sheshukova, J.-Y. Duquesne, M. Marangolo, G. Csaba *et al.*, The 2021 magnonics roadmap, J. Phys.: Condens. Matter **33**, 413001 (2021).

[31] M. M. Nayga, S. Rachel, and M. Vojta, Magnon Landau levels and emergent supersymmetry in strained antiferromagnets, Phys. Rev. Lett. **123**, 207204 (2019).

[32] D. L. Esteras, A. Rybakov, A. M. Ruiz, and J. J. Baldoví, Magnon straintronics in the 2D van der Waals ferromagnet CrSBr from first-principles, Nano Lett. **22**, 8771 (2022).

[33] I. Tsubokawa, On the magnetic properties of a $CrBr_3$ single crystal, J. Phys. Soc. Jpn. **15**, 1664 (1960).

[34] M. A. McGuire, G. Clark, S. KC, W. M. Chance, G. E. Jellison, V. R. Cooper, X. Xu, and B. C. Sales, Magnetic behavior and spin-lattice coupling in cleavable van der Waals layered $CrCl_3$ crystals, Phys. Rev. Mater. **1**, 014001 (2017).

[35] W. Jin, H. H. Kim, Z. Ye, S. Li, P. Rezaie, F. Diaz, S. Siddiq, E. Wauer, B. Yang, C. Li, S. Tian, K. Sun, H. Lei, A. W. Tsen, L. Zhao, and R. He, Raman fingerprint of two terahertz spin wave branches in a two-dimensional honeycomb Ising ferromagnet, Nat. Commun. **9**, 5122 (2018).

[36] F. J. Dyson, General theory of spin-wave interactions, Phys. Rev. **102**, 1217 (1956).

[37] S. Maleev, Scattering of slow neutrons in ferromagnets, Sov. Phys. JETP **6**, 776 (1958).

[38] F. J. Dyson, Thermodynamic behavior of an ideal ferromagnet, Phys. Rev. **102**, 1230 (1956).

[39] H. H. Kim, B. Yang, S. Li, S. Jiang, C. Jin, Z. Tao, G. Nichols, F. Sfigakis, S. Zhong, C. Li, S. Tian, D. G. Cory, G.-X. Miao, J. Shan, K. F. Mak, H. Lei, K. Sun, L. Zhao, and A. W. Tsen, Evolution of interlayer and intralayer magnetism in three atomically thin chromium trihalides, Proc. Natl. Acad. Sci. USA **116**, 11131 (2019).

[40] See Supplemental Material at http://link.aps.org/supplemental/10.1103/PhysRevResearch.6.013210 for the Dirac magnon spectrum, the width dependent pseudomagnetic field and the first magnon Landau level energy.

[41] B. Wei, J.-J. Zhu, Y. Song, and K. Chang, Renormalization of gapped magnon excitation in monolayer $MnBi_2Te_4$ by magnon-magnon interaction, Phys. Rev. B **104**, 174436 (2021).

[42] V. V. Mkhitaryan and L. Ke, Self-consistently renormalized spin-wave theory of layered ferromagnets on the honeycomb lattice, Phys. Rev. B **104**, 064435 (2021).

[43] A. H. C. Neto, F. Guinea, N. M. R. Peres, K. S. Novoselov, and A. K. Geim, The electronic properties of graphene, Rev. Mod. Phys. **81**, 109 (2009).

[44] R. M. Menezes, D. Šabani, C. Bacaksiz, C. C. de Souza Silva, and M. V. Milošević, Tailoring high-frequency magnonics in monolayer chromium trihalides, 2D Mater. **9**, 025021 (2022).

[45] S. P. Koenig, N. G. Boddeti, M. L. Dunn, and J. S. Bunch, Ultrastrong adhesion of graphene membranes, Nat. Nanotechnol. **6**, 543 (2011).

[46] A. Castellanos-Gomez, R. Roldán, E. Cappelluti, M. Buscema, F. Guinea, H. S. J. van der Zant, and G. A. Steele, Local strain engineering in atomically thin MoS_2, Nano Lett. **13**, 5361 (2013).

[47] S. Zhu, J. A. Stroscio, and T. Li, Programmable extreme pseudomagnetic fields in graphene by a uniaxial stretch, Phys. Rev. Lett. **115**, 245501 (2015).

[48] D. Lloyd, X. Liu, J. W. Christopher, L. Cantley, A. Wadehra, B. L. Kim, B. B. Goldberg, A. K. Swan, and J. S. Bunch, Band gap engineering with ultralarge biaxial strains in suspended monolayer MoS_2, Nano Lett. **16**, 5836 (2016).

[49] G. Wang, Z. Dai, J. Xiao, S. Z. Feng, C. Weng, L. Liu, Z. Xu, R. Huang, and Z. Zhang, Bending of multilayer van der Waals materials, Phys. Rev. Lett. **123**, 116101 (2019).

[50] F. Meier and D. Loss, Magnetization transport and quantized spin conductance, Phys. Rev. Lett. **90**, 167204 (2003).